

Wave–Current Interactions at Meso- and Submesoscales: Insights from Idealized Numerical Simulations^❶

ANA B. VILLAS BÔAS,^a BRUCE D. CORNUELLE,^a MATTHEW R. MAZLOFF,^a
SARAH T. GILLE,^a AND FABRICE ARDHUIN^{b,a}

^a Scripps Institution of Oceanography, University of California, San Diego, La Jolla, California

^b IFREMER, Univ. Brest, CNRS, IRD, Laboratoire d’Océanographie Physique et Spatiale, Brest, France

(Manuscript received 9 July 2020, in final form 20 September 2020)

ABSTRACT: Surface gravity waves play a major role in the exchange of momentum, heat, energy, and gases between the ocean and the atmosphere. The interaction between currents and waves can lead to variations in the wave direction, frequency, and amplitude. In the present work, we use an ensemble of synthetic currents to force the wave model WAVEWATCH III and assess the relative impact of current divergence and vorticity in modifying several properties of the waves, including direction, period, directional spreading, and significant wave height H_s . We find that the spatial variability of H_s is highly sensitive to the nature of the underlying current and that refraction is the main mechanism leading to gradients of H_s . The results obtained using synthetic currents were used to interpret the response of surface waves to realistic currents by running an additional set of simulations using the llc4320 MITgcm output in the California Current region. Our findings suggest that wave parameters could be used to detect and characterize strong gradients in the velocity field, which is particularly relevant for the Surface Water and Ocean Topography (SWOT) satellite as well as several proposed satellite missions.

KEYWORDS: Ocean; Sea/ocean surface; Atmosphere-ocean interaction; Mesoscale processes; Waves, oceanic; Numerical analysis/modeling

1. Introduction

Surface waves are part of the physical boundary that separates the ocean from the atmosphere, mediating exchanges of momentum, heat, energy, gases, and other tracers between these two media (Cavaleri et al. 2012; Villas Bôas et al. 2019). Waves are modulated by ocean currents via wave–current interactions, which lead to variations in their direction, frequency, and amplitude (Phillips 1966; Peregrine 1976). The effects of ocean currents on surface waves have been observed across upwelling jets off the California coast and meanders in the Loop Current region (Romero et al. 2017; Romero 2019). These modulations resulted in high spatial inhomogeneity of the wave field, enhancing nonlinear effects such as wave breaking and producing variations of up to 30% in the significant wave height H_s (the average of the highest one-third of the wave heights). Moreover, recent case studies based on realistic numerical simulations in the Gulf Stream and the Drake Passage suggest that surface currents dominate the variability of H_s at scales between 10 and 100 km (Ardhuin et al. 2017). Although there is growing observational evidence based on satellite measurements to support this hypothesis (e.g., Quilfen et al. 2018;

Quilfen and Chapron 2019), our knowledge of how meso- and submesoscale currents affect the surface wave field is still limited by the lack of simultaneous measurements of waves and currents at these scales.

The surface kinetic energy (KE) of the ocean at mesoscales is known to be dominated by nondivergent, geostrophically balanced motions; however, in the submesoscale range, divergent motions associated with fronts, tides, and inertia-gravity waves account for a large portion of the KE (Bühler et al. 2014; Rocha et al. 2016a; McWilliams 2016). Several studies motivated by the upcoming Surface Water and Ocean Topography (SWOT) satellite altimetry mission have found strong seasonality in the KE in many regions of the ocean (e.g., Qiu et al. 2018, 2017; Rocha et al. 2016b). In the California Current System (CCS) region, for example, the KE is mostly dominated by balanced (rotational) motions in late winter/spring, while divergence is stronger in late summer/fall (Chereskin et al. 2019). Recent theoretical work by Villas Bôas and Young (2020, hereinafter VBY20) shows from a ray-tracing framework that surface waves respond remarkably differently to divergent and rotational flows. Thus, a seasonality in the underlying kinematics governing surface currents should result in significant changes in the surface wave field.

Ardhuin et al. (2017) found strong gradients in wave heights associated with the flow intensity and structure. In that study, the authors used realistic currents, waves, and wind forcing to investigate relationships between currents and waves. More recently, Romero et al. (2020) investigated the effects of currents on waves using very high-resolution $O(100)$ m currents from a setup of the ocean model ROMS in Southern California to force the Wave Height, Water Depth, and Current Hindcasting (WAVEWATCH III) third generation wave model (hereinafter

^❶ Denotes content that is immediately available upon publication as open access.

Supplemental information related to this paper is available at the Journals Online website: <https://doi.org/10.1175/JPO-D-20-0151.s1>.

Corresponding author: Ana B. Villas Bôas, avillasboas@ucsd.edu

WW3). Although their results suggest wave refraction to be the main cause of H_s gradients, the underlying mechanisms leading to that are difficult to isolate due to the complexity of their model, which encompasses interactions between currents, winds, waves and other sources and sinks of wave action. In this context, idealized simulations provide a useful tool to diagnose the mechanisms leading to gradients in the wave field and to shed light on the extent to which surface wave gradients could be used to infer kinematic properties of the flow.

Building on [Ardhuin et al. \(2017\)](#) and the theoretical framework from [VBY20](#), here we analyze a large ensemble of numerical experiments produced using an idealized setup of WW3 forced by synthetic currents to assess how the wave field responds to rotational and divergent flows. In addition, the response behavior diagnosed with the synthetic currents is used to interpret the results of simulations using realistic currents from a high-resolution ocean model in the CCS region. In [section 2](#), we present a theoretical background on current effects on waves. [Section 3](#) describes the methods and the wave model setup. Results are presented and discussed in [section 4](#). Finally, a summary of the main results and conclusions of this paper is presented in [section 5](#).

2. Background

In this section we provide some theoretical background on the effects of currents on waves. We focus on linear deep-water surface gravity waves and, for the purpose of this paper, we consider horizontal currents that are depth independent, i.e., there is no vertical shear. Here, we are only concerned about the effects of currents on waves and not the effects of waves on currents. For a recent description of the two-way coupled problem see, for example, [McWilliams \(2018\)](#) and [Suzuki \(2019\)](#).

Waves propagating over a current are subject to a Doppler shift of their frequency, which can be expressed as

$$\omega(t, \mathbf{x}, \mathbf{k}) = \sigma + \mathbf{k} \cdot \mathbf{U}(t, \mathbf{x}), \quad (1)$$

where ω is the absolute frequency (as observed from a fixed reference frame), σ is the intrinsic frequency (as observed from a reference frame moving with the current), $\mathbf{k} = (k_1, k_2)$ is the wavenumber vector, and $\mathbf{U}(t, \mathbf{x}) = (u, v)$ is the horizontal surface current. The intrinsic frequency is related to the wavenumber via the dispersion relationship. The cases studied here use the dispersion relationship for deep-water linear surface waves:

$$\sigma = (gk)^{1/2}, \quad (2)$$

where g is the gravitational acceleration and $k = |\mathbf{k}|$. Here, the effects of surface currents on waves will be explored in the light of ray theory for linear waves, which assumes the geometrical optics approximation. For doing so, the underlying assumption is that currents are slowly varying with respect to the waves, i.e., the temporal scales of variations in the current field are longer and the spatial scales are larger than those of the waves. Formally, one can express these assumptions as (e.g., [Peregrine 1976](#)):

$$k \gg \max \left| \frac{1}{U} \frac{\partial U}{\partial L_U} \right| \quad \text{and} \quad \omega \gg \max \left| \frac{1}{U} \frac{\partial U}{\partial T_U} \right|, \quad (3)$$

where U is the characteristic current speed, and L_U and T_U are the characteristic spatial and temporal scales of the current. In addition, the group speed of the waves $c = (1/2)(g/k)^{1/2}$ is assumed to be much larger than the current speed U , such that

$$\varepsilon \stackrel{\text{def}}{=} \frac{U}{c} \ll 1. \quad (4)$$

Using index notation, in which subscripts after the comma indicate partial derivatives, the evolution of the absolute frequency, wavenumber, and trajectory following a wave train are then given by the ray equations:

$$\dot{\omega} = k_n \partial_t U_n, \quad (5a)$$

$$\dot{k}_n = -\partial_{x_n} \omega = -U_{m,n} k_m, \quad (5b)$$

$$\dot{x}_n = \partial_{k_n} \omega = c_n + U_n, \quad (5c)$$

where $c_n = \partial_{k_n} \sigma(k)$ is the group velocity, and the overdot represents the total time derivative following the wave train:

$$\dot{\partial}_t + (U_n + c_n) \partial_{x_n}. \quad (6)$$

The sea state is composed of waves of multiple frequencies and directions, such that a convenient way of describing it is through the wave energy density spectrum $E(t, \mathbf{x}, \mathbf{k})$. However, under the influence of an inhomogeneous current, the wave energy is not conserved, due to the exchange of energy between the currents and the wave field via radiation stresses ([Longuet-Higgins and Stewart 1961, 1962](#)). Instead, the wave action A , here approximated as $A(t, \mathbf{x}, \mathbf{k}) = E(t, \mathbf{x}, \mathbf{k})/\sigma$, is conserved ([Bretherton and Garrett 1968; Phillips 1966](#)). Then, the dynamical aspects of the evolution of the wave field can be described by the conservation of wave action:

$$\dot{\partial}_t A + \dot{x}_n \partial_{x_n} A + \dot{k}_n \partial_{k_n} A = S, \quad (7)$$

where \dot{x}_n and \dot{k}_n are given by [\(5c\)](#) and [\(5b\)](#), and S represents sources and sinks of wave action such as wave breaking, nonlinear interactions, and wind forcing.

In the context of numerical wave modeling, the wavenumber vector is often decomposed into magnitude k and direction θ , such that $A(t, \mathbf{x}, \mathbf{k}) \equiv A(t, \mathbf{x}, k, \theta)$, and [\(7\)](#) can be written as

$$\dot{\partial}_t A + (\mathbf{U} + \mathbf{c}) \cdot \nabla A + \dot{k} \partial_k A + \dot{\theta} \partial_\theta A = S, \quad (8)$$

where ∇ is the horizontal gradient operator. In [\(8\)](#), the first term on the left-hand side represents local changes of wave action; the second term is the advection of wave action in physical space (x, y) by the Doppler-shifted group velocity ($\mathbf{U} + \mathbf{c}$); the last two terms represent the advection of wave action in spectral space (k, θ), where the third term is associated with changes in wavenumber (or frequency), and the fourth term is associated with changes in wave direction (refraction).

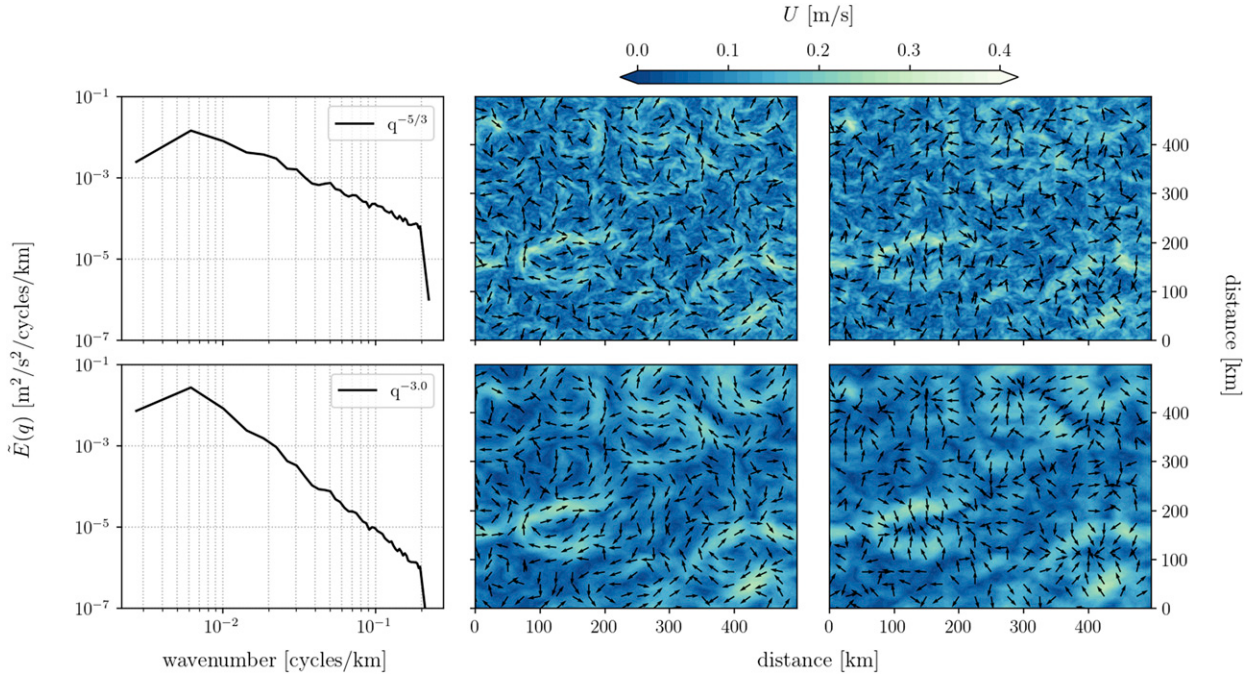


FIG. 1. Example of stochastic velocity fields with a prescribed spectral slope and random phase. (top) The isotropic kinetic energy spectrum for a flow with (left) a $q^{-5/3}$ spectral slope and the corresponding velocity field for (center) a purely rotational flow (\mathbf{U}^ψ) and (right) a purely divergent flow (\mathbf{U}^ϕ). (bottom) As in the top row, but for a spectral slope of q^{-3} .

3. Methods

a. Current forcing

1) SYNTHETIC CURRENT FIELDS

According to Helmholtz's theorem of vector calculus, any sufficiently smooth two-dimensional velocity field can be decomposed into a component that is purely divergent (\mathbf{U}^ϕ , described by a velocity potential ϕ) and a component that is purely rotational (\mathbf{U}^ψ , described by a streamfunction ψ), such that the sum of the two components reconstructs the original velocity completely:

$$\mathbf{U} = \mathbf{U}^\phi + \mathbf{U}^\psi, \quad (9)$$

where

$$\mathbf{U}^\phi = (\phi_x, \phi_y), \quad \text{and} \quad \mathbf{U}^\psi = (-\psi_y, \psi_x). \quad (10)$$

We generate a set of stochastic horizontal velocity fields as follows. First, a two-dimensional scalar field with prescribed isotropic spectral slope and random phase is created. Then, this field is used as both a velocity potential and as a streamfunction to obtain \mathbf{U}^ϕ and \mathbf{U}^ψ from (10). The resulting divergent and rotational components of the velocity have isotropic kinetic energy spectra $\tilde{E}^\phi(q)$ and $\tilde{E}^\psi(q)$ that follow a q^{-S} power law, where $q = |\mathbf{q}|$ is the horizontal isotropic wavenumber of the flow and S is the respective spectral slope. Additionally, the velocities are constructed such that all the variance of the flow is contained in wavelengths between 5 and 300 km. To represent spectral slopes of surface kinetic energy that are typically

observed in the ocean at meso- and submesoscales (e.g., Rocha et al. 2016a,b; Qiu et al. 2018), we limit our parameter space to spectral slopes of $S = (5/3, 2, 2.5, 3)$. Figure 1 shows an example of synthetic \mathbf{U}^ψ (center column) and \mathbf{U}^ϕ (right column) and the respective kinetic energy spectra for a shallow spectral slope ($q^{-5/3}$, top) and a steep spectral slope (q^{-3} , bottom).

The final velocity used in our simulations is obtained by combining the rotational and divergent components of the flow and normalizing the mean kinetic energy (KE) such that

$$\mathbf{U}_n = \alpha^{1/2} \mathbf{U}_n^\phi + (1 - \alpha)^{1/2} \mathbf{U}_n^\psi, \quad (11)$$

and, given the orthogonality of the cross terms,

$$\begin{aligned} \text{KE} &= \frac{1}{2} \langle \mathbf{U}_n^2 \rangle = \alpha \underbrace{\frac{1}{2} \langle (u^\phi)^2 + (v^\phi)^2 \rangle}_{\text{KE}^\phi} + (1 - \alpha) \underbrace{\frac{1}{2} \langle (u^\psi)^2 + (v^\psi)^2 \rangle}_{\text{KE}^\psi} \\ &= \alpha \text{KE}^\phi + (1 - \alpha) \text{KE}^\psi, \end{aligned} \quad (12)$$

$$(13)$$

where α is a number between zero and one that corresponds to the fraction of the total mean KE accounted for by the divergent component of the flow. So, if $\alpha = 1$ the flow is purely divergent, and if $\alpha = 0$ the flow is purely rotational. We ran experiments with α ranging from 0 to 1 at increments of 0.2. For a particular realization of random phases, the combination of the four different values of S and six different values of α results in 24 possible velocity fields.

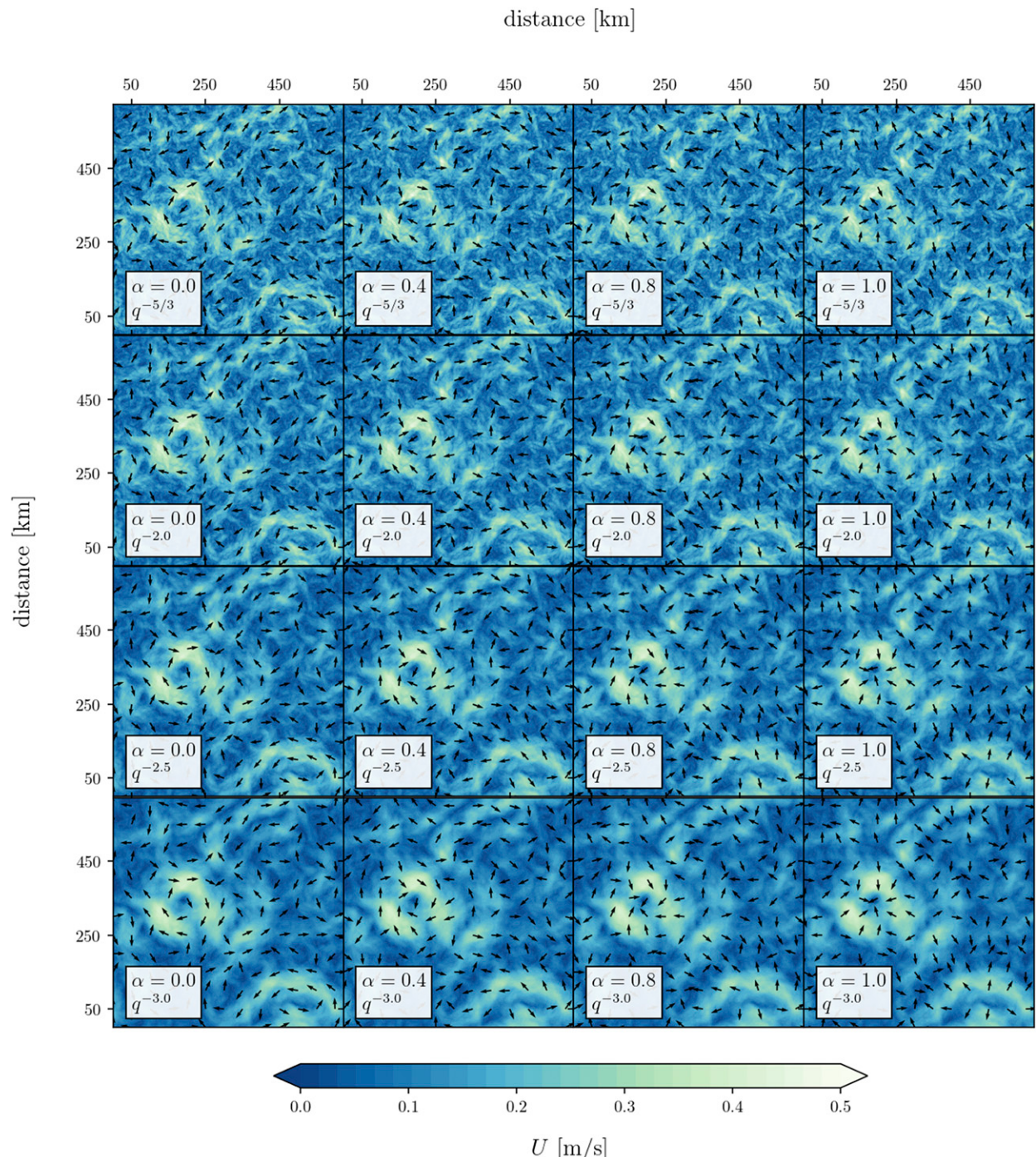


FIG. 2. One realization of synthetic velocity fields created using the method described in section 1. From left to right the velocities go from being purely rotational ($\alpha = 0$) to being purely divergent ($\alpha = 1$). From top to bottom the respective kinetic energy spectral slope goes from $q^{-5/3}$ to q^{-3} . All panels have the same mean kinetic energy and phase.

For clarity, most of the discussion in the following sections focuses on cases using $\alpha = (0, 0.4, 0.8, 1)$ since we find that these values represent the behavior of the entire range. An example of one realization of a synthetic current field is shown in Fig. 2.

2) REALISTIC CURRENTS FROM THE MITGCM LLC4320

To investigate the response of surface waves to realistic mesoscale and submesoscale currents, we used snapshots of surface velocity from the latitude-longitude polar cap

TABLE 1. Parameter space used for the simulations with synthetic currents. The combination of these parameters result in 72 possibilities that are each run 50 times, yielding a total of 3600 model runs.

	Parameter space					
Divergence fraction (α)	0.0	0.2	0.4	0.6	0.8	1.0
Spectral slope (\S)	-5/3	-2.0	-2.5	-3.0		
Wave mean period ($T_{m0,-1}$)	7.0 s	10.3 s	16.6 s			

numerical simulation llc4320 (Rocha et al. 2016a) which has nominal resolution of $1/48^\circ$ and was obtained using the Massachusetts Institute of Technology general circulation model (MITgcm). The llc4320 was forced by tides and by 6-hourly surface atmospheric fields. Here, we use surface velocities from the llc4320 in the CCS region ($28^\circ\text{--}35^\circ\text{N}$ and $120^\circ\text{--}129^\circ\text{W}$) from October 2011 to September 2012 that were interpolated onto a 2.5 km regular Cartesian grid on a $600\text{ km} \times 600\text{ km}$ domain. These velocity fields were then subsampled every 6 h and used as an ensemble of snapshots (i.e., no temporal evolution) to force the wave model as described below.

b. Experimental setup

We use version 5.16 of the wave model WW3 (WAVEWATCH III Development Group 2016) to integrate the action balance equation. Here, we are only interested in the effects of currents on freely propagating swell-type waves, which are distant from their generation site. Additionally, the waves considered here have small steepness and are far from approaching the breaking limit. With that in mind, we neglect wind forcing, nonlinear interactions, and wave breaking, which effectively means that the right-hand side of (8) is zero. Throughout this paper we discuss wave quantities that are averaged over the wave energy spectrum, which are known as “bulk” quantities. In particular, we focus on the significant wave height H_s , mean direction θ_w , mean period $T_{m0,-1}$, and directional spreading σ_θ , which are formally defined in the appendix. All simulations are initialized with a narrow-banded wave spectrum of short-crested waves which is Gaussian in frequency and has a cosine directional distribution. Waves enter the domain from the left boundary with initial mean direction $\theta_w = 270^\circ$ (propagating from left to right), directional spreading $\sigma_\theta = 12.4^\circ$, and $H_s = 1\text{ m}$. We run cases with initial mean period $T_{m0,-1} = (7, 10.3, 16.6\text{ s})$ that are characteristic of swell. Although the quantitative results are affected by the initial value of the directional spreading, the overall discussion remains valid within a range of σ_θ characteristic of swell. Thus, in this manuscript, we chose a fixed value for the initial directional spreading and leave the detailed dependency of the results on σ_θ for future studies.

The experiments are run on a $600\text{ km} \times 600\text{ km}$ Cartesian domain with 2.5-km spatial grid resolution, 32 frequencies, and 48 directions. We use a global integration time step of 200 s, spatial advection time step of 50 s, spectral advection time step of 12 s, and minimum source term time step of 5 s (see the appendix for more detail on the model setup). Increasing the spectral resolution or decreasing the time stepping does not change the results (not shown). The boundary condition at the left boundary is kept constant throughout the experiment and

each experiment is run until steady state is reached, which takes on average the time for a wave of period $T_{m0,-1}$ to cross the domain (0.5–1.3 days). For the WW3 configuration used here, numerical errors are small enough such that in control cases without current forcing, all bulk quantities of the wave field in the entire domain are uniform, constant, and equal to the boundary condition, with standard deviation on the order of 10^{-6} for all variables (not shown). In other words, without currents, H_s would be equal to 1 m, θ_w would be equal to 270° , σ_θ would be equal to 12.4° , and $T_{m0,-1}$ would be equal to the chosen boundary condition mean period, everywhere. We refer the reader to the appendix for a list of switches used to compile WW3.

To explore how different properties of the flow affect the wave field, we force WW3 in the configuration described above using an ensemble of synthetic surface currents created as described in section 1. Each realization of this ensemble consists of 24 possible cases (see Table 1) that are run for three initial different values of $T_{m0,-1}$, yielding a total of 72 possible cases per realization. We run 50 realizations, which corresponds to a total of 3600 experiments. In addition, the response of the wave field to realistic currents is assessed using surface currents from the llc4320 to force the same WW3 setup. Without loss of generality, we only ran simulations with an initial mean period of 10.3 s with the llc4320 currents.

4. Results

a. Spatial variability of bulk wave parameters

We begin by analyzing the spatial variability of bulk quantities of the wave field, namely, mean direction, significant wave height, mean period, and directional spreading. For the sake of clarity, here we discuss snapshots from WW3 forced by one realization of synthetic currents with $\text{KE} = 0.01\text{ m}^2\text{ s}^{-2}$ and for waves with initial mean period of 10.3 s, although the same discussion applies for the entire ensemble. Each figure is organized as follows:

- Along a fixed row, all panels were forced with currents that have the same kinetic energy spectrum $\tilde{E}(q)$ and different divergence fractions α , which increases from $\alpha = 0$ (left, purely rotational) to $\alpha = 1$ (right, purely divergent).
- Along a fixed column, all panels were forced with currents that have the same divergence fraction and different kinetic energy spectral slope, which varies from a shallow slope (top, $q^{-5/3}$) to a steep slope (bottom, q^{-3}).
- The results are interpreted as deviations from a simulation with no current forcing, in which all bulk quantities are uniform and equal across all panels (i.e., all panels would be entirely filled with the same color).

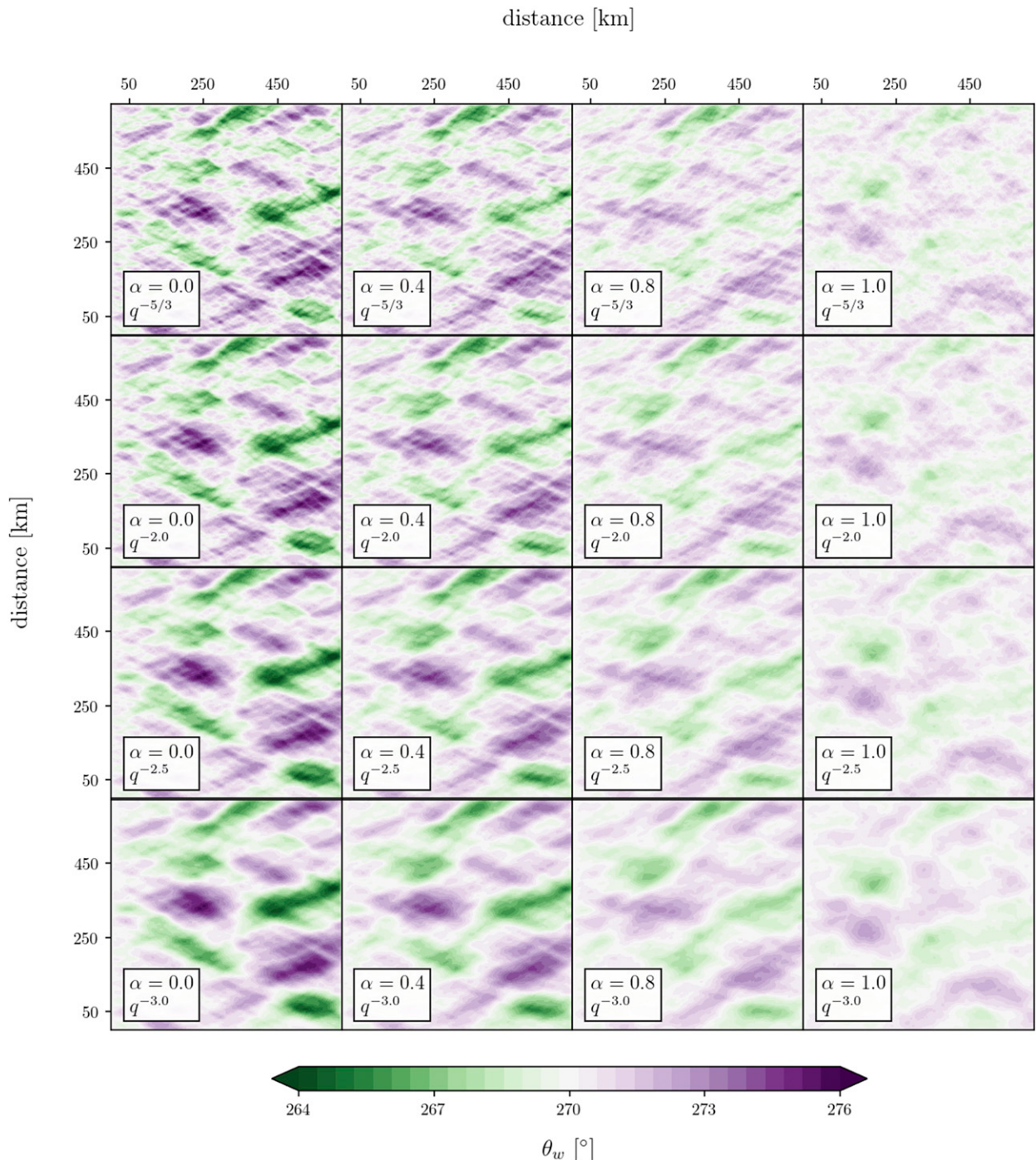


FIG. 3. Mean direction θ_w for one realization of the idealized simulations spanning the entire parameter space, which consists of four spectral slopes ($q^{-5/3}, q^{-2}, q^{-2.5}, q^{-3}$) and four divergence fractions $\alpha = (0, 0.4, 0.8, 1)$, where $\alpha = 0$ corresponds to a purely rotational flow and $\alpha = 1$ to a purely divergent flow. For a case without currents, θ_w would be equal to 270° in the entire domain.

1) MEAN DIRECTION

Figure 3 shows snapshots of mean direction θ_w . Close to the left boundary, θ_w is nearly uniform and equal to the boundary condition at the left boundary ($\theta_w = 270^\circ$). As the waves

propagate through the domain, the currents may modify the mean direction at a given location by both refraction and advection of wave action (where the latter effect is of order ε). Refraction is larger for cases where the currents are mostly rotational (first two columns) than cases where currents are

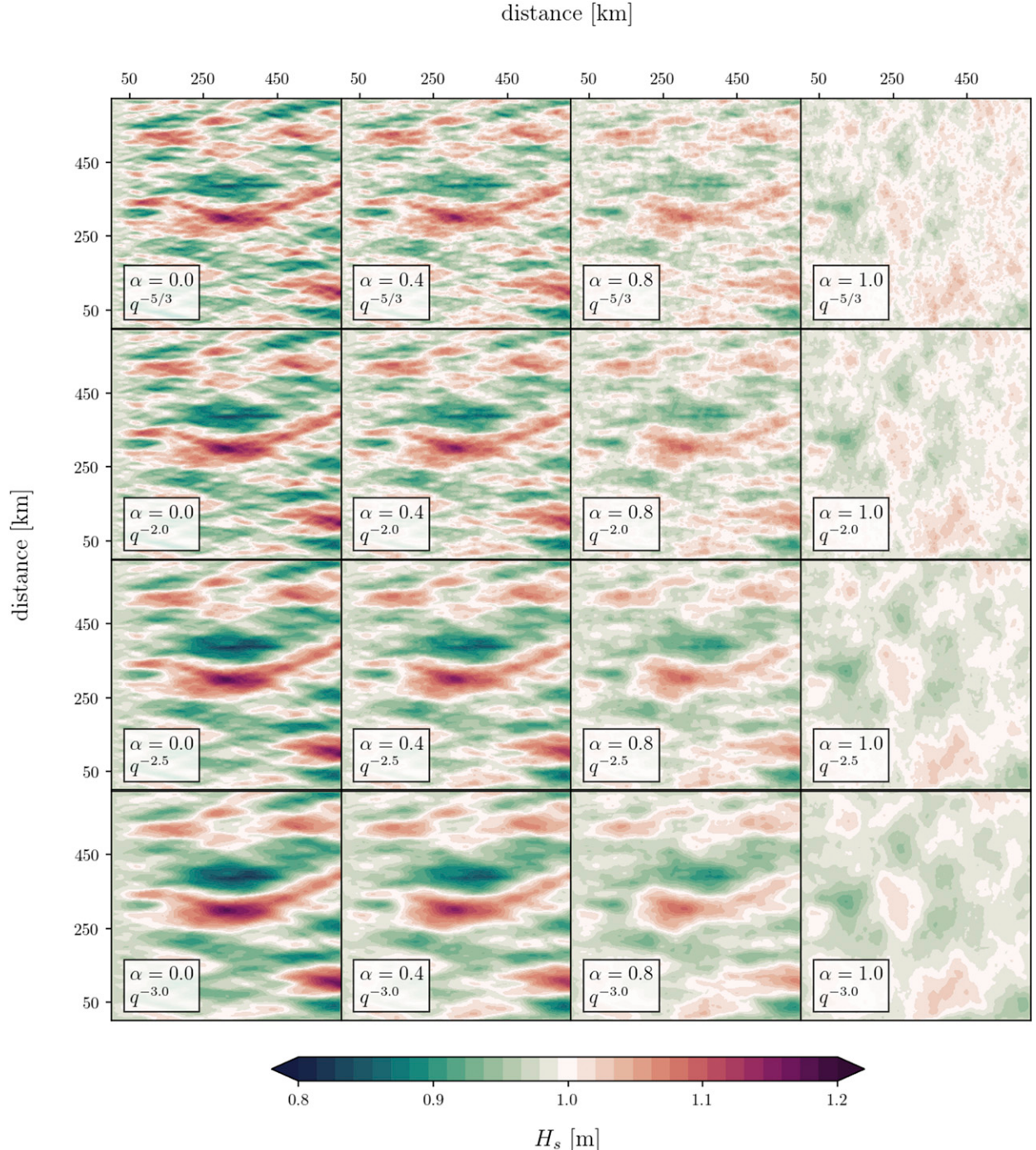


FIG. 4. As in Fig. 3, but for the significant wave height H_s . For a case without currents, H_s would be equal to 1 m in the entire domain for all panels.

mostly divergent (last two columns). This result is consistent with the predictions from ray theory: in the limit of weak currents one can approximate the curvature of individual rays (how much the rays refract) by the ratio between the vorticity ζ of the flow and the group velocity of the waves (Kenyon 1971; Landau and Lifshitz 1987; Dysthe 2001). Thus, in the last

column where the flow is purely divergent ($\zeta = 0$), θ_w does not deviate much from the initial condition. Although we only show snapshots from one realization, the discussion above applies to the entire ensemble. For waves that have $T_{m0,-1} = 10.3$ s, the standard deviation of the θ_w across all realizations decreases from $\approx 2^\circ$ when $\alpha = 0$ to $\approx 0.7^\circ$ when $\alpha = 1$, for all spectral slopes.

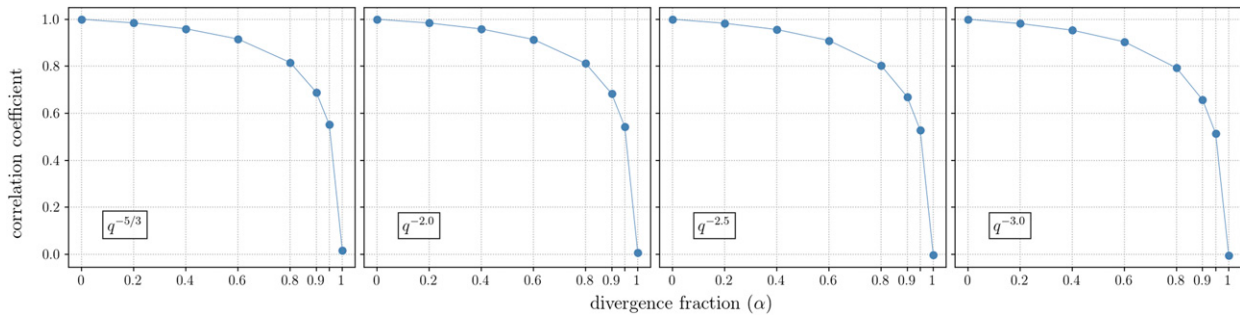


FIG. 5. Correlation coefficient as a function of α between the significant wave height for the case $\alpha = 0$ and all other cases. Each panel corresponds to a different spectral slope. The correlation coefficients for each value of α were averaged across 20 realizations. The standard error of the mean is too small to be noticeable on the plot.

2) SIGNIFICANT WAVE HEIGHT

Strong refraction leads to strong convergences and divergences of wave action, which result in spatial gradients of significant wave height (Fig. 4). As a consequence, gradients of H_s are stronger in the first two columns (where the flow has more vorticity) than in the last two columns (where the flow has more divergence). For these purely rotational currents that have $KE = 0.01 \text{ m}^2 \text{ s}^{-2}$ and waves with $T_{m0,-1}$ on the order of 10 s, we observe a change of up to 20% in H_s at scales of tens of kilometers. Additionally, visual inspection of Fig. 4 show that current fields with shallow spectral slope (top two rows) result in variability of H_s at shorter spatial scales in comparison to steep spectral slopes (bottom two rows) suggesting a scale dependency between the current forcing and the wave response.

A striking feature of Fig. 4 is the abrupt change in the spatial variability of H_s from $\alpha = 0.8$ to 1. In the first three columns, increasing the divergence fraction (going from left to right) results in weaker gradients of H_s but with a similar spatial pattern in each column. However, the picture changes completely when the flow is purely divergent (last column). To better characterize this transition, we have run two additional sets of simulations with $\alpha = 0.9$ and $\alpha = 0.95$. Figure 5 shows the spatial correlation of H_s between the case with $\alpha = 0$ and all other values of α . Regardless of the spectral slope, the correlation drops from about 0.5 for $\alpha = 0.95$ to zero for $\alpha = 1$, which means that even if only 5% of the kinetic energy of the flow is in the rotational component, the spatial variability of H_s is still remarkably similar to the purely rotational case.

3) MEAN PERIOD

Why is the spatial variability of H_s for the purely divergent case in Fig. 4 so different from the other cases? For the purely divergent case ($\alpha = 1$) the vorticity is zero, and refraction no longer dominates the action balance equation. Conservation of the absolute frequency $\omega = \sigma + \mathbf{k} \cdot \mathbf{U}$ leads to a change of order ε in the intrinsic frequency, which in turn changes the wave energy via conservation of wave action. Then, in terms of bulk parameters, an increase in $T_{m0,-1}$ would correspond to a decrease in H_s for action to be conserved. Figure 6 shows the mean period for the respective cases discussed in Figs. 3 and 4. Comparing Figs. 4 and 6, we can see that the spatial pattern of H_s in the purely divergent case (Fig. 4, last column) nearly

matches the spatial pattern of the mean period (Fig. 6, last column). More specifically, blue regions in the last column of Fig. 6 (decrease in $T_{m0,-1}$) correspond to red regions in Fig. 4 (increase in H_s). Computing the spatial correlation between H_s and $T_{m0,-1}$ for $\alpha = 1.0$ and averaging across all realizations results in correlation coefficients of -0.72 , -0.73 , -0.77 , and -0.81 for $S = 5/3$, 2 , 2.5 , and 3 , respectively. Additionally, a back-of-the-envelope calculation (see Phillips 1966, p. 74) using a current speed variation on the order of 0.5 m s^{-1} (as in Fig. 2) and group velocity of 8 m s^{-1} (corresponding to $T_{m0,-1} = 10.3 \text{ s}$) leads to a change of 3% in $T_{m0,-1}$ and a corresponding change of about 6% in H_s , which is in agreement with the values observed in the last column of Figs. 4 and 6.

4) DIRECTIONAL SPREADING

Figure 7 shows snapshots of the directional spreading σ_θ . Waves enter the domain from the left boundary with an initial directional spreading of 12.4° . As the waves propagate through the domain they are refracted by the currents which results in higher directional spreading, increasing from left ($x = 0 \text{ km}$) to right ($x = 600 \text{ km}$) on each panel. As shown in Fig. 3, more vorticity leads to stronger refraction; thus σ_θ is higher for the purely rotational flow (first column, $\alpha = 0$), and it decreases as α increases. Figure 7 also reveals that shallower spectral slopes (top two rows) produce higher directional spreading than steep spectral slopes (bottom two rows). Perhaps the most interesting feature of Fig. 7 is the fact that there is virtually no change in the directional spreading for purely divergent flows (last column, $\alpha = 1$). Using a ray tracing approach, VBY20 have recently shown that the divergent component of the flow has no contribution to the directional diffusion of wave action. Our results corroborate the VBY20 results in a spectral wave modeling framework. VBY20 arrived at an analytical expression for the variance of the wave direction that depends on the kinetic energy spectrum of the rotational component of the flow only and also found larger directional variance for shallow spectral slopes. Although there is no direct relationship between the direction of monochromatic wave rays and the mean direction computed from a wave spectrum, the directional spreading [as defined in (A4)] provides an energy-weighted proxy for the variance of wave direction discussed by VBY20.

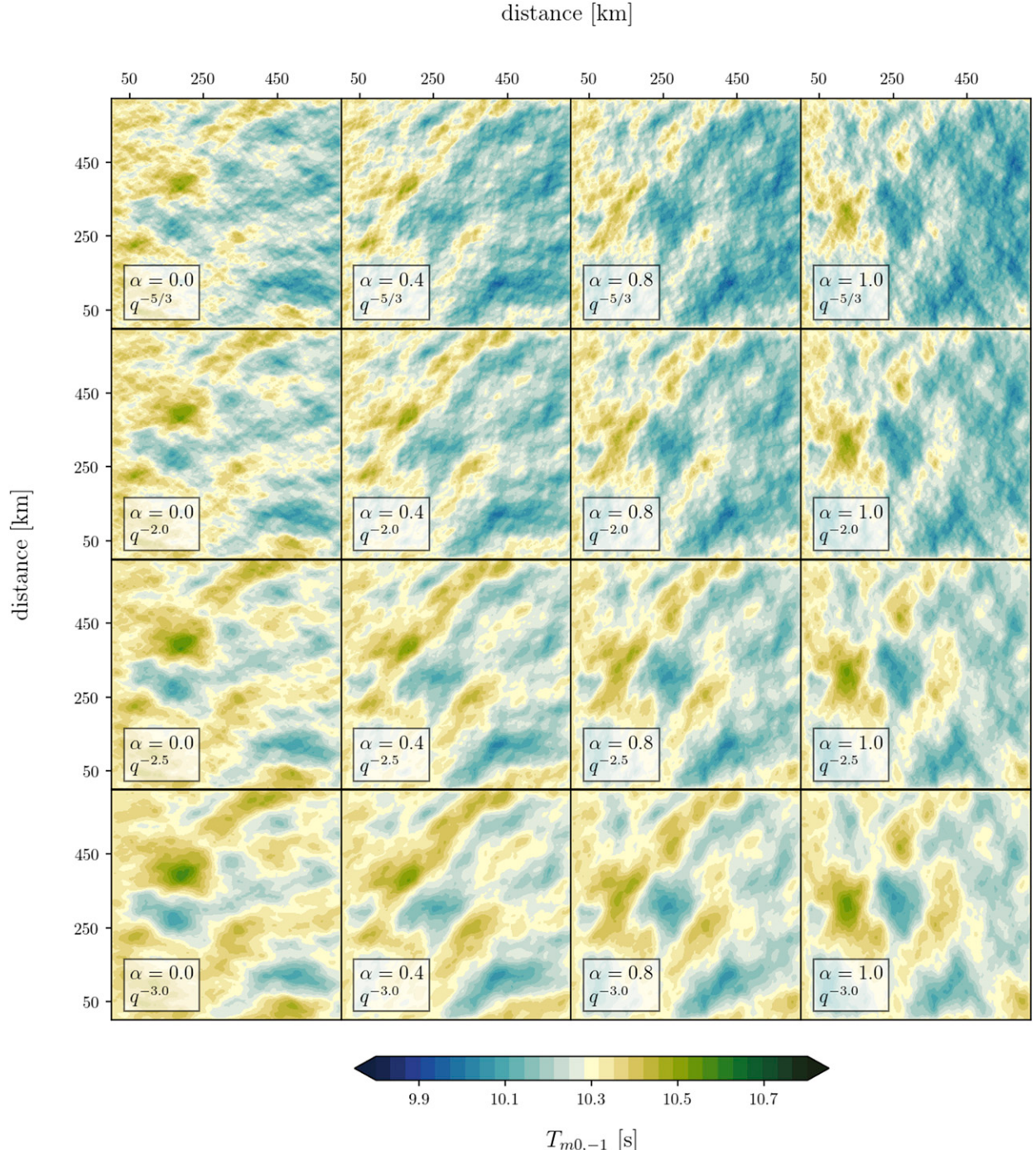


FIG. 6. As in Fig. 3, but for the mean period $T_{m0,-1}$. In the absence of currents, $T_{m0,-1}$ would be equal to 10.3 s in the entire domain for all panels.

b. Significant wave height response to vorticity and divergence

1) SYNTHETIC CURRENTS

So far we have seen that spatial gradients of H_s are stronger for cases where most of the kinetic energy of the flow is in the

rotational component (Fig. 4) and that this coincides with the cases where refraction is also stronger (Fig. 3). Building on the results from VBY20 that found no directional diffusion of wave action by the divergent component of the flow and what we have shown in section 4a, we hypothesize that the spatial variability of H_s is determined by the spatial variability of the

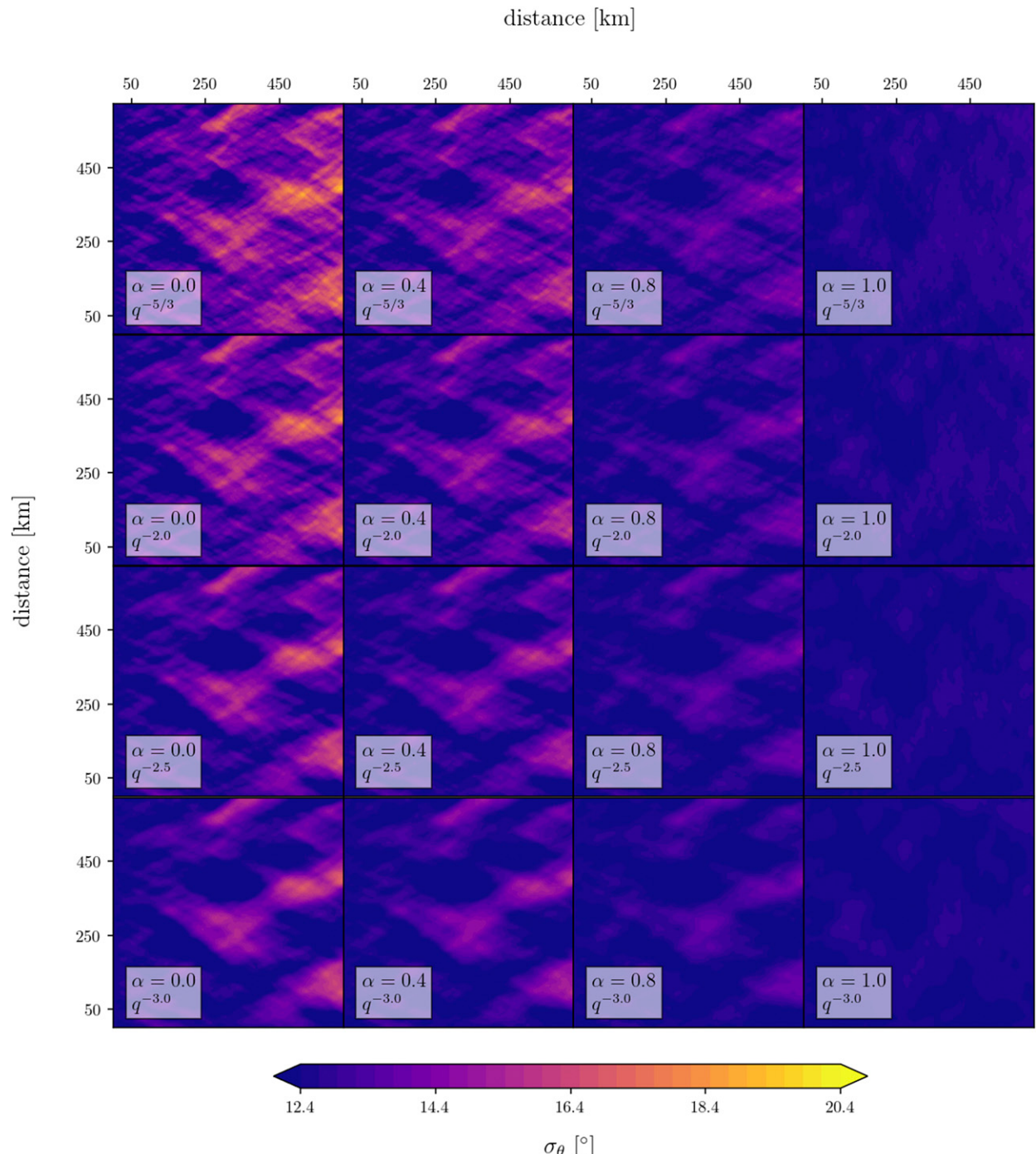


FIG. 7. As in Fig. 3, but for the directional spreading σ_θ . In the absence of currents, σ_θ would be equal to 12.4° in the entire domain for all panels.

rotational component of the flow. To test this hypothesis we run an additional set of experiments in which we double the kinetic energy of the purely rotational flow by adding an equally energetic potential component. One realization of such an experiment (for $S = 2.5$) is shown in Fig. 8. In Fig. 8a the flow is purely rotational with $KE = 0.01 \text{ m}^2 \text{ s}^{-2}$. In Fig. 8b $KE =$

$0.02 \text{ m}^2 \text{ s}^{-2}$, where the rotational component was kept the same and the additional energy was obtained by adding a purely divergent flow to Fig. 8a. One would expect that stronger currents would have a larger impact on the wave field; however, the respective H_s responses (Figs. 8c,d) are fairly similar (rms difference of 0.01 m), providing evidence that the spatial

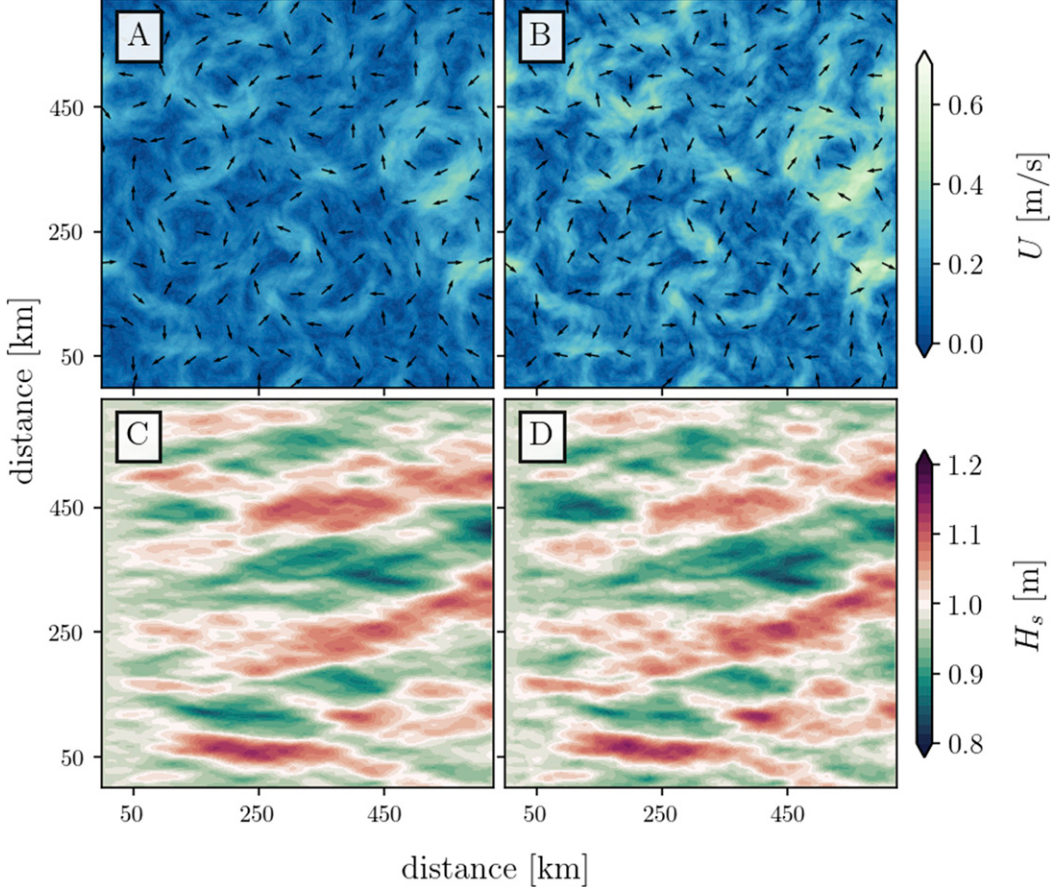


FIG. 8. (a),(b) Surface current forcing and (c),(d) respective significant wave heights H_s . In (a) the flow is purely rotational ($\alpha = 0$) and has KE = $0.01 \text{ m}^2 \text{ s}^{-2}$ which produces the H_s shown in (c). The flow in (b) was obtained by adding a purely divergent component to (a), resulting in a current twice as energetic (KE = $0.02 \text{ m}^2 \text{ s}^{-2}$) with $\alpha = 0.5$ and corresponding H_s shown in (d). In both cases the flow has a kinetic energy spectral slope $S = 2.5$.

variability of H_s at these scales is not affected by the potential component of the flow.

To further verify our hypothesis, we ran 50 realizations of experiments with the same setup as the example shown in Fig. 8 and computed the average wavenumber spectra of surface currents and significant wave heights for all kinetic energy spectral slopes considered in this study. Although the flow is isotropic, it is clear from the snapshots of H_s (Fig. 8) that the surface wave response is not, since the experimental setup produces waves propagating in a preferential direction (from left to right). Thus, instead of using the isotropic spectrum, we analyze the one-dimensional wavenumber spectrum as a function of the q_2 wavenumber, obtained by integrating the 2D spectra in the q_1 wavenumber direction

$$\tilde{E}(q_2) = \int \tilde{E}(\mathbf{q}) dq_1, \quad (14)$$

where $\tilde{E}(q_2)$ is the one-dimensional spectrum and $\mathbf{q} = (q_1, q_2)$ is the horizontal wavenumber vector. Additionally, to avoid the transition region close to the left boundary, where the

statistics are not yet stationary, we neglect the first 200 km of the domain when computing the wavenumber spectra.

Figure 9 confirms our hypothesis that, to leading order, the spatial variability of H_s is not affected by the divergent component of the flow. Although we forced the wave model with currents that are twice as energetic (dashed black), the resulting wavenumber spectra of H_s (dashed green) are indistinguishable from the purely rotational case (solid green) and this is true for all spectral slopes. Another remarkable feature to note in Fig. 9 is that at scales between 15 and 200 km (gray shaded box) the spectral slope of H_s nearly follows the KE spectral slope, meaning that shallow H_s spectral slopes are associated with shallow KE slopes (e.g., $q^{-5/3}$), while steep H_s spectral slopes are associated with steep KE slopes (e.g., q^{-3}).

2) REALISTIC CURRENT FORCING

A question that naturally arises from the results discussed up to this point of this manuscript is if the same behavior would be observed for realistic currents. A detailed analysis of the seasonality of kinetic energy at submesoscales in the CCS was recently carried out by Chereskin et al. (2019) using both

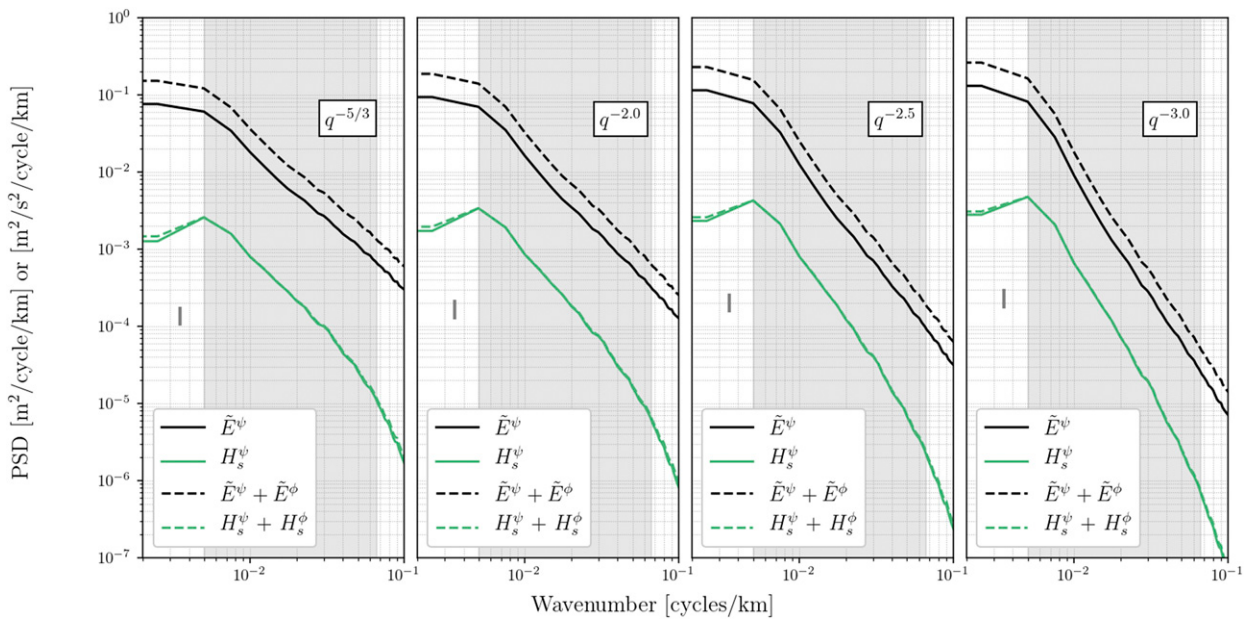


FIG. 9. Wavenumber spectra of kinetic energy for a purely rotational flow with $\text{KE} = 0.01 \text{ m}^2 \text{ s}^{-2}$ (E^ψ , solid black) and combined rotational and potential flow with $\text{KE} = 0.02 \text{ m}^2 \text{ s}^{-2}$ ($E^\psi + E^\phi$, dashed black). Each panel shows different spectral slopes as indicated in the upper box. The respective wavenumber spectra for the significant wave height are shown in green, solid for the purely rotational case (H_s^ψ) and dashed for the combined rotational and potential ($H_s^\psi + H_s^\phi$). These 1D spectra were obtained by integrating the 2D spectra in the q_1 wavenumber direction, thus representing the variance density as a function of the q_2 wavenumber. The spectra were averaged across 50 realizations, and the error bar is shown as a light gray line. For clarity, the H_s spectra were scaled by a factor of 10^{-1} . The gray shaded box indicates the wavelength range between 200 and 15 km.

observational data and the output from the llc4320 simulation. The authors show that in this region, KE is dominated by balanced motions (rotational) in late winter/spring, whereas internal waves and other divergent motions dominate the KE in summer/fall. From our experiments with idealized currents, we expect the spatial variability of H_s to respond to the rotational component of the flow. Thus, a seasonality in the rotational KE in the CCS region, should lead to a seasonality in the H_s wavenumber spectrum, whereas changes in the divergent component of the KE should not significantly change the H_s spectrum.

To test this hypothesis, an equivalent setup was used to run WW3 forced with realistic currents from the MITgcm llc4320 in the CCS region, as explained in section 2. Figure 10 shows snapshots of surface relative vorticity (top) from the llc4320 in the winter (left) and summer (right) and the H_s (bottom) obtained from WW3 forced with the respective llc4320 currents. In the winter, strong vorticity results in strong gradients in H_s that are comparable with the values obtained for small α in Fig. 4 (up to 20% change in H_s). In contrast, H_s gradients in the summer are much weaker as a consequence of a weak vorticity field. This example illustrates how the seasonality of the submesoscale in the CCS may affect surface waves leading to strong seasonality in the variations of gradients of H_s .

For the following analysis, we applied a Helmholtz decomposition to separate the rotational and divergent components of the llc4320 currents (e.g., Bühler et al. 2014; Rocha et al. 2016a). We start by considering January and July as examples.

The top left panel of Fig. 11 shows KE spectra of the rotational (\tilde{E}^ψ) component of the flow in January (solid blue) and July (solid red). In agreement with the results from Chereskin et al. (2019), we observe higher values of \tilde{E}^ψ in January at all wavenumbers. In contrast, the KE spectra of the divergent component \tilde{E}^ϕ (Fig. 11, top right) do not change much between these two months. Now, if we focus on the significant wave height spectra (dashed), we see that the H_s spectrum is also more energetic in January (blue), particularly at scales between 200 and 15 km (shaded box). Since \tilde{E}^ϕ is nearly constant between January and July, we conclude that the observed change in the H_s spectrum is caused by the KE in the rotational component of the flow.

We can further analyze this problem by looking at the opposite case: we choose two months where there is a significant difference in the divergent component of the KE, but the rotational component remains somewhat constant. The bottom two panels of Fig. 11 illustrate this scenario. Between October (purple) and March (orange), \tilde{E}^ψ is relatively constant at scales between 200 and 15 km (Fig. 11, bottom-left panel); however, \tilde{E}^ϕ is much larger in October than March (Fig. 11, bottom-right panel). Despite \tilde{E}^ϕ being larger in October, the H_s spectra do not change significantly between October and March reinforcing the idea that divergent component of the flow does not affect the spatial variability of H_s .

Considering that for the waves analyzed in this paper (narrow-banded swell), the dominant balance in the conservation of wave action in (8) is between advection (second term

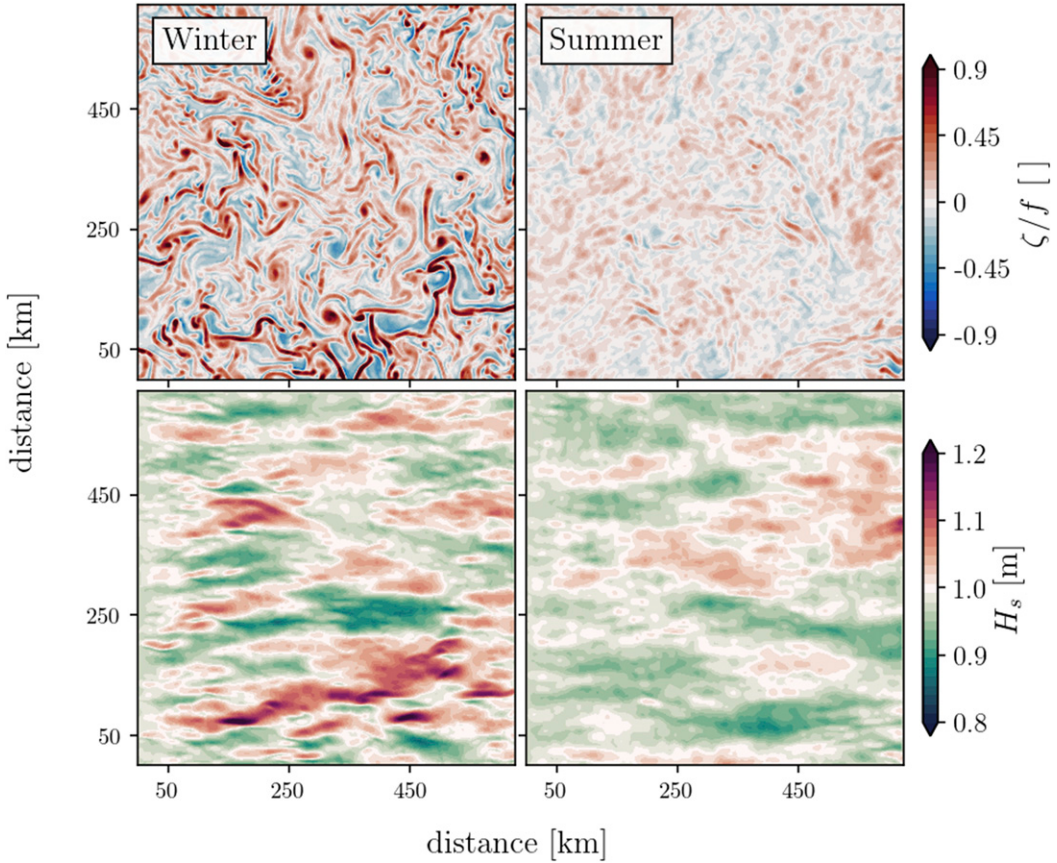


FIG. 10. (top) Snapshots of surface relative vorticity from the llc4320 in the (left) winter and (right) summer and (bottom) the significant wave height H_s obtained from WW3 forced by the respective llc4320 currents. The vorticity is normalized by the local Coriolis parameter. Note that the color scale for H_s is the same used in the previous plots.

on the left-hand side) and refraction (last term on the left-hand side), we expect a relationship between spatial gradients of significant wave height and the vertical vorticity of the flow. Applying these scaling arguments to (8) allows us to arrive at the following relation (see the online supplemental material for more details):

$$c \frac{|\nabla H_s|_{\text{rms}}}{\langle H_s \rangle} \propto \mathbb{S} \zeta_{\text{rms}}, \quad (15)$$

where c is the group speed, $|\nabla H_s|_{\text{rms}}$ is the root-mean-square (rms) significant wave height gradient, $\langle H_s \rangle$ is the mean significant wave height, \mathbb{S} is the spectral slope of the flow, and ζ_{rms} is the rms vertical vorticity of the flow.

Figure 12 illustrates the scaling (15): results for experiments using both synthetic (dots) and realistic (crosses) currents all collapse to the same line (see Fig. S1 in the online supplemental material for sequential illustrations of the collapse). In Fig. 12, light blue dots were computed from the ensemble described in Table 1 that have mean KE = $0.01 \text{ m}^2 \text{s}^{-2}$. Dark blue dots correspond to a total of 480 realizations of experiments with the same parameter space as in Table 1, but with KE = $0.005 \text{ m}^2 \text{s}^{-2}$ and only for waves with initial $T_{m0,-1} = 10.3 \text{ s}$. Note that all cases with $\alpha = 1.0$, for which the vorticity is zero,

were excluded from this analysis. Black crosses correspond to experiments forced by the llc4320 currents, for which the spectral slope, divergence fraction, and mean kinetic energy are not prescribed. The experiments using the llc4320 currents are also only for waves with initial $T_{m0,-1} = 10.3 \text{ s}$ and correspond to a total of 1464 realizations. The right-hand side of (15) is scaled by the kinetic energy spectral slope \mathbb{S} . The concept of a spectral slope for the llc4320 currents is subjective, and here it was estimated by doing a linear fit (in log space) to each spectrum between wavelengths of 10 and 100 km.

The relationship in (15) synthesizes the idea that spatial gradients of H_s are caused by vorticity, and it provides a direct connection between bulk wave quantities (left-hand side) and kinematic properties of the flow (right-hand side) that applies to a wide range of currents and wave conditions. For all three cases shown in Fig. 12, the correlation coefficient is greater than 0.9.

We have shown that surface waves contain information on statistical properties of the flow, such as the kinetic energy spectrum and the rms vorticity. Now, do surface wave gradients contain phase information of current gradients? If we go back to the limit of a monochromatic wave with propagation described by the ray equations, the evolution of the wave direction can be written as

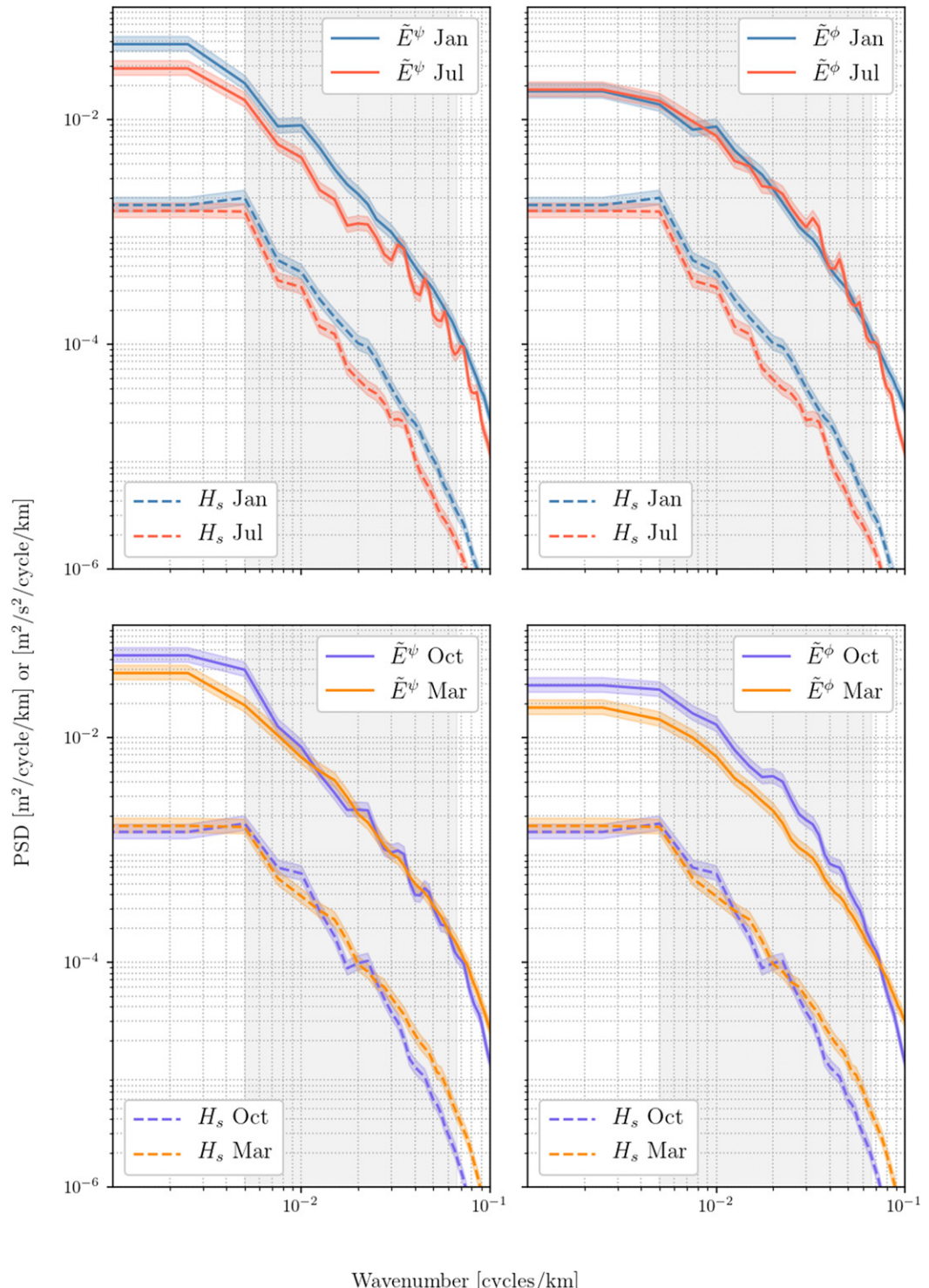


FIG. 11. Wavenumber spectra of KE from the MITgcm llc4320 (solid), and the respective spectra of significant wave height H_s (dashed). The spectra are shown as monthly averages for January (blue), July (red), October (purple), and March (orange). The KE spectra (left) for the rotational component of the flow (\tilde{E}^ψ) and (right) for the divergent component (\tilde{E}^ϕ). To facilitate the comparison, the same H_s spectra is plotted both on the left and right panels. All H_s spectra were scaled by a factor of 10^{-1} . The color shades represent the 95% confidence limit. The gray shaded box indicates the wavelength range between 200 and 15 km.

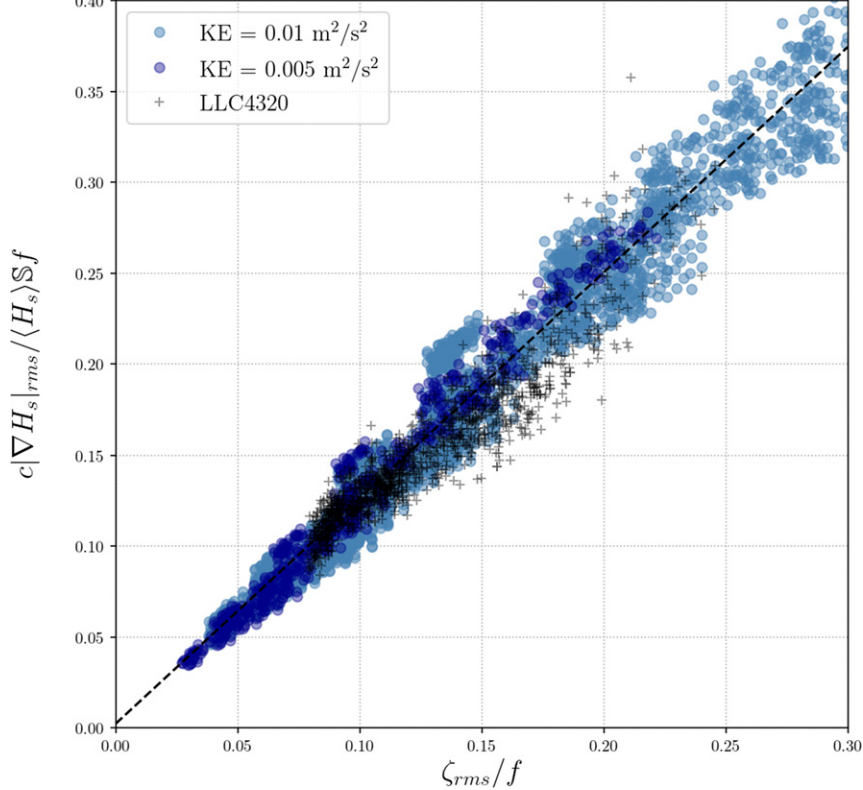


FIG. 12. Scatterplot of nondimensional rms significant wave height gradient as a function of normalized rms vorticity. Light blue dots are from the ensemble described in Table 1, that have mean $\text{KE} = 0.01 \text{ m}^2 \text{ s}^{-2}$. Dark blue dots correspond to a total of 480 realizations of experiments with the same parameter space as in Table 1, but with $\text{KE} = 0.005 \text{ m}^2 \text{ s}^{-2}$ and only for waves with initial $T_{m0,-1} = 10.3 \text{ s}$. Black crosses correspond to experiments forced by the llc4320 currents, for which the spectral slope, divergence fraction, and mean kinetic energy are not prescribed. The experiments using the llc4320 currents are also only for waves with initial $T_{m0,-1} = 10.3 \text{ s}$ and correspond to a total of 1464 realizations. For this plot, both sides of (15) were normalized by the mean Coriolis parameter in the CCS region ($f = 7.8 \times 10^{-5}$) for all realizations.

$$\theta_t + (\mathbf{U} + \mathbf{c}) \cdot \nabla \theta = -\frac{1}{k} \hat{\mathbf{n}} \cdot \nabla (\mathbf{k} \cdot \mathbf{U}), \quad (16)$$

where $\hat{\mathbf{n}}$ is a unit vector in the direction perpendicular to the wavenumber \mathbf{k} . We remind the reader that we are considering the steady-state solution with $\varepsilon = U/c \ll 1$, so defining $\nabla_{\parallel} \stackrel{\text{def}}{=} \hat{\mathbf{k}} \cdot \nabla$ and $\nabla_{\perp} \stackrel{\text{def}}{=} \hat{\mathbf{n}} \cdot \nabla$ as the gradient in the direction parallel and perpendicular to the wavenumber direction, respectively, we can write (16) to $O(\varepsilon)$ as

$$c \nabla_{\parallel} \theta = -\nabla_{\perp} U^k, \quad (17)$$

where U^k is the component of \mathbf{U} in the direction of the wavenumber \mathbf{k} (along-wave). Equation (17) says that, for monochromatic waves, if we know the wave direction and group velocity everywhere, we can retrieve the gradient of the along-wave component of the current in the direction perpendicular to the wave propagation.

Figure 13a shows a snapshot of surface speed from the llc4320 where we observe a sharp diagonal front on the right

side of the domain. Now, we apply (17) to a narrow-banded wave spectrum using the group velocity at the mean period ($c = gT_{m0,-1}/4\pi$) and the mean wave direction ($\theta = \theta_w$). Figure 13b shows the gradient of the along-wave component of the current in the direction perpendicular to the mean direction and is our “truth,” meaning that Fig. 13b was computed straight from the llc4320 currents. Note that the front described in Fig. 13a appears in Fig. 13b as a diagonal line in shades of blue. Figure 13c shows the same gradient as in Fig. 13b, but now computed using the left-hand side of (17), which depends only on wave quantities. In other words, without any knowledge of the current field, a “beam” of short-crested, narrow-banded waves is able to provide insight on the spatial structure of current gradients. For the case shown in Fig. 13, the spatial correlation coefficient between Figs. 13b and 13c is on the order of 0.6. Similar analysis was performed for all llc2320 current snapshots. Because refraction is a nonlocal effect, we expect the skill of (17) to be higher close to the left boundary and decrease as the waves propagate through the domain.

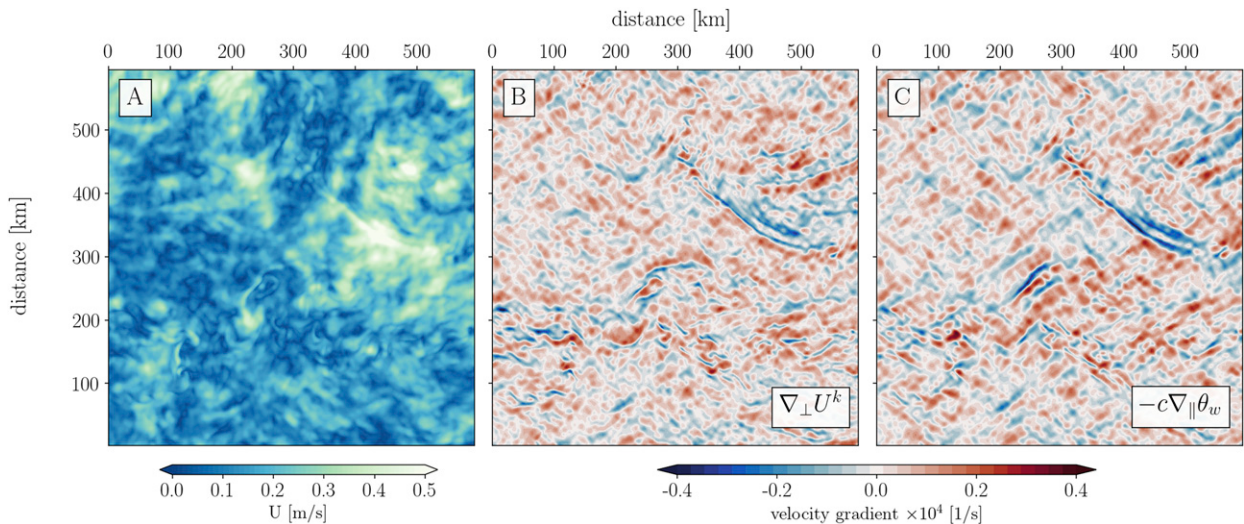


FIG. 13. (a) Snapshot of surface speed from the llc4320; (b) gradient of the along-wave component of the current shown in (a) in the direction perpendicular to the wave propagation [see Eq. (17)]; (c) group velocity at the mean period multiplied by the gradient of the mean wave direction in the direction parallel to the wave propagation. Note that the sharp diagonal front on the right side of (a) appears as a dark blue diagonal line both in (b) and (c).

Additionally, we also expect the skill to vary seasonally, depending on the relative contribution of the rotational and divergent part to the surface kinetic energy. This inhomogeneity in the skill of (17) was quantified through the correlation coefficient shown in Fig. S2.

5. Summary and conclusions

An ensemble of synthetic currents were used to force WAVEWATCH III and assess the relative importance of current divergence and vorticity in modifying several properties of the wave field. Using these idealized numerical simulations we were able to show that the spatial variability of the significant wave height is driven by the rotational component of the flow, which is the only component that has vorticity. For the type of waves considered in this paper, which have relatively long period and are not subject to wind forcing, we found refraction to be the main mechanism leading to spatial gradients of wave heights. These findings corroborate the results from Arduin et al. (2017), who have done experiments turning the refraction term on and off in the wave model as opposed to controlling the vorticity in the currents, as well as the observational results from Quilfen and Chapron (2019). Further, we have also shown that purely divergent flows do not contribute to increasing the directional spreading of the wave field, which extends the results from VBY20 to a narrow-banded wave spectrum.

Gradients of wave quantities contain information about statistical and kinematic properties of the flow. In particular, we have shown that the wavenumber spectrum of the significant wave height is highly sensitive to the nature of the underlying current. Our numerical results suggest that at scales from 15 to 200 km the spectral slope of H_s follows the spectral slope of the rotational component of the surface kinetic

energy and, most remarkably, that variance of H_s is not affected by the kinetic energy contained in the divergent component of the flow.

The upcoming SWOT mission will measure the sea surface height (SSH) with the unprecedented spatial resolution of tens of kilometers. While conventional satellite altimetry has for decades provided us with a quasi-global picture of the ocean's geostrophic circulation, deriving velocities from SSH will pose a challenge for SWOT since at the SWOT scales, divergent (nongeostrophic) motions associates with tides, internal waves, and fronts may contribute to a significant portion of the SSH signal (Morrow et al. 2019). In response to that, community efforts have focused on strategies to separate balanced from unbalanced motions. One of the main takeaways from this paper is that surface waves respond differently to rotational (balanced) and divergent (unbalanced) flows, which may offer the possibility of using the wave information contained in the SWOT signal to help distinguish between these two dynamical regimes.

In addition to the synthetic current forcing, a set of idealized simulations with realistic currents from the MITgcm llc4320 model was run. Our results using the llc4320 demonstrate that waves are modulated by ocean currents over the scales of eddies and fronts even with the comparatively weak currents of the California Current System [$U < 0.5 \text{ m s}^{-1}$ and $\zeta = O(f)$]. As a consequence, we observed that in the CCS region seasonal differences in the dominant regime and spatial scales of the background flow led to corresponding differences in H_s . Note that in a realistic scenario, the wave field itself would also experience a seasonal variability that is not associated with the currents. Here, we have focused on only the wave response to the seasonality of the currents.

Finally, the highly structured wave response to coherent features present in the llc4320 currents offers the possibility of

using wave parameters to detect and characterize strong gradients in the velocity field. The case illustrated here relies on a “beam” of narrow banded swell and requires knowledge of the spatial variability of the wave frequency and direction. Understanding how surface waves respond to currents in a more realistic scenario and the extent to which wave information could be used to constrain ocean currents calls for joint observations of winds, currents, and waves. Efforts such as NASA’s Sub-Mesoscale Ocean Dynamics Experiment (S-MODE; [Farrar et al. 2020](#)) and Doppler oceanography satellite mission concepts such as the Winds and Currents Mission (WACM; [Rodríguez et al. 2019](#)) and the Sea Surface Kinematics Multiscale Monitoring (SKIM; [Ardhuin et al. 2019](#)) will be of paramount importance to our understanding of how meso- and submesoscale currents affect waves.

Acknowledgments. We thank the two anonymous reviewers for their comments and suggestions. ABVB was funded by NASA Earth and Space Science Fellowship award number 80NSSC17K0326. ABVB, STG, MRM, and BDC were funded by NASA awards NNX16AH67G and 80NSSC20K1136). ABVB and FA acknowledge the Kavli Institute for Theoretical Physics for partially supporting this research through the National Science Foundation Grant No. NSF PHY17-48958. FA was partially funded by the Office of Naval Research grant N00014-17-1-2402. ABVB first discussed the idea of running this set of experiments with Ken Melville, who was on her PhD committee before he passed away. Ken was a giant in the field of surface waves, and she feels extremely grateful for having had the chance to work with him. This paper is dedicated to him.

Data availability statement. All model output analyzed in this paper is available from <https://doi.org/10.6075/J0X928V6>. The source code used to produce the figures can be accessed on GitHub: <https://github.com/biavillasboas/IdealizedWaveCurrent>.

APPENDIX

WAVEWATCH III Setup and Bulk Parameters

In this manuscript we used WAVEWATCH III version 5.16 compiled with the following switches: F90, NOGRB, NOPA, LRB4, SCRIP, SCRIPNC, NC4, TRKNC, DIST, MPI, PR3, UQ, FLX0, LN1, ST4, STAB0, NL1, BT0, DB0, TR0, BS0, IC0, IS0, REF0, IGO, XX0, WNT2, WNX1, RWND, CRT1, CRX1, O0, O1, O2, O2a, O2b, O2c, O3, O4, O5, O6, and O7.

The spectral grid used had 48 directions (7.5° resolution) and 32 frequencies with the lowest frequency equal to 0.041 18 Hz and an increment factor of 1.1.) The spatial grid had 2.5-km resolution in both x and y and we used a global integration time step of 200 s, spatial advection time step of 50 s, spectral advection time step of 12 s, and minimum source term time step of 5 s.

The wave field was described using bulk parameters, which are computed within WW3 from integrals of the wave energy spectrum. Below is the formal definition of these parameters. For more details on the bulk parameters calculation and the

numerical schemes used by WW3 we refer the reader to the WW3 user manual ([WAVEWATCH III Development Group 2016](#)).

a. Significant wave height H_s

The significant wave height H_s is defined as

$$H_s = 4\sqrt{E}, \quad (\text{A1})$$

where

$$E = \int_0^{2\pi} \int_0^{\infty} E(\sigma, \theta) d\sigma d\theta. \quad (\text{A2})$$

b. Mean period $T_{m0,-1}$

The mean period $T_{m0,-1}$ is the energy-weighted average of the wave period defined as

$$T_{m0,-1} = \frac{1}{E} \int_0^{2\pi} \int_0^{\infty} \sigma^{-1} E(\sigma, \theta) d\sigma d\theta. \quad (\text{A3})$$

c. Directional spreading σ_θ

Directional spreading σ_θ is defined as

$$\sigma_\theta = \left\{ 2 \left[1 - \left(\frac{a^2 + b^2}{E^2} \right)^{1/2} \right] \right\}^{1/2}, \quad (\text{A4})$$

where

$$a = \int_0^{2\pi} \int_0^{\infty} \cos\theta E(\sigma, \theta) d\sigma d\theta, \quad (\text{A5})$$

and

$$b = \int_0^{2\pi} \int_0^{\infty} \sin\theta E(\sigma, \theta) d\sigma d\theta. \quad (\text{A6})$$

d. Mean direction θ_w

The mean direction θ_w is defined as

$$\theta_w = \text{atan}\left(\frac{b}{a}\right). \quad (\text{A7})$$

REFERENCES

- Ardhuin, F., S. T. Gille, D. Menemenlis, C. B. Rocha, N. Rasle, B. Chapron, J. Gula, and J. Molemaker, 2017: Small-scale open ocean currents have large effects on wind wave heights. *J. Geophys. Res. Oceans*, **122**, 4500–4517, <https://doi.org/10.1002/2016JC012413>.
- , and Coauthors, 2019: SKIM, a candidate satellite mission exploring global ocean currents and waves. *Front. Mar. Sci.*, **6**, 209, <https://doi.org/10.3389/FMARS.2019.00209>.
- Bretherton, F. P., and C. J. Garrett, 1968: Wavetrains in inhomogeneous moving media. *Proc. Roy. Soc. London*, **302A**, 529–554, <https://doi.org/10.1098/rspa.1968.0034>.
- Bühler, O., J. Callies, and R. Ferrari, 2014: Wave–vortex decomposition of one-dimensional ship-track data. *J. Fluid Mech.*, **756**, 1007–1026, <https://doi.org/10.1017/jfm.2014.488>.

- Cavaleri, L., B. Fox-Kemper, and M. Hemer, 2012: Wind waves in the coupled climate system. *Bull. Amer. Meteor. Soc.*, **93**, 1651–1661, <https://doi.org/10.1175/BAMS-D-11-00170.1>.
- Chereskin, T. K., C. B. Rocha, S. T. Gille, D. Menemenlis, and M. Passaro, 2019: Characterizing the transition from balanced to unbalanced motions in the southern California current. *J. Geophys. Res. Oceans*, **124**, 2088–2109, <https://doi.org/10.1029/2018JC014583>.
- Dysthe, K. B., 2001: Refraction of gravity waves by weak current gradients. *J. Fluid Mech.*, **442**, 157–159, <https://doi.org/10.1017/S0022112001005237>.
- Farrar, J. T., and Coauthors, 2020: S-mode: The submesoscale ocean dynamics experiment. *2020 IEEE International Geoscience and Remote Sensing Symp.*, Waikoloa, Hawaii, IEEE, WE2.R8.4, https://igarss2020.org/view_paper.php?PaperNum=2115.
- Kenyon, K. E., 1971: Wave refraction in ocean currents. *Deep-Sea Res. Oceanogr. Abstr.*, **18**, 1023–1034, [https://doi.org/10.1016/0011-7471\(71\)90006-4](https://doi.org/10.1016/0011-7471(71)90006-4).
- Landau, L. D., and E. M. Lifshitz, 1987: *Fluid Mechanics*. 2nd ed. Course of Theoretical Physics, Vol. 6, Elsevier, 266 pp.
- Longuet-Higgins, M. S., and R. Stewart, 1961: The changes in amplitude of short gravity waves on steady non-uniform currents. *J. Fluid Mech.*, **10**, 529–549, <https://doi.org/10.1017/S0022112061000342>.
- , and —, 1962: Radiation stress and mass transport in gravity waves, with application to ‘surf beats’. *J. Fluid Mech.*, **13**, 481–504, <https://doi.org/10.1017/S0022112062000877>.
- McWilliams, J. C., 2016: Submesoscale currents in the ocean. *Proc. Roy. Soc.*, **472A**, 20160117, <https://doi.org/10.1098/rspa.2016.0117>.
- , 2018: Surface wave effects on submesoscale fronts and filaments. *J. Fluid Mech.*, **843**, 479–517, <https://doi.org/10.1017/jfm.2018.158>.
- Morrow, R., and Coauthors, 2019: Global observations of fine-scale ocean surface topography with the Surface Water and Ocean Topography (SWOT) mission. *Front. Mar. Sci.*, **6**, 232, <https://doi.org/10.3389/fmars.2019.00232>.
- Peregrine, D., 1976: Interaction of water waves and currents. *Advances in Applied Mechanics*, Vol. **16**, Elsevier, 9–117.
- Phillips, O., 1966: *The Dynamics of the Upper Ocean*. Cambridge University Press, 269 pp.
- Qiu, B., T. Nakano, S. Chen, and P. Klein, 2017: Submesoscale transition from geostrophic flows to internal waves in the northwestern Pacific upper ocean. *Nat. Commun.*, **8**, 14055, <https://doi.org/10.1038/ncomms14055>.
- , S. Chen, P. Klein, J. Wang, H. Torres, L.-L. Fu, and D. Menemenlis, 2018: Seasonality in transition scale from balanced to unbalanced motions in the world ocean. *J. Phys. Oceanogr.*, **48**, 591–605, <https://doi.org/10.1175/JPO-D-17-0169.1>.
- Quilfen, Y., and B. Chapron, 2019: Ocean surface wave-current signatures from satellite altimeter measurements. *Geophys. Res. Lett.*, **46**, 253–261, <https://doi.org/10.1029/2018GL081029>.
- , M. Yurovskaya, B. Chapron, and F. Ardhuin, 2018: Storm waves focusing and steepening in the agulhas current: Satellite observations and modeling. *Remote Sens. Environ.*, **216**, 561–571, <https://doi.org/10.1016/j.rse.2018.07.020>.
- Rocha, C. B., T. K. Chereskin, S. T. Gille, and D. Menemenlis, 2016a: Mesoscale to submesoscale wavenumber spectra in Drake Passage. *J. Phys. Oceanogr.*, **46**, 601–620, <https://doi.org/10.1175/JPO-D-15-0087.1>.
- , S. T. Gille, T. K. Chereskin, and D. Menemenlis, 2016b: Seasonality of submesoscale dynamics in the Kuroshio extension. *Geophys. Res. Lett.*, **43**, 11 304–11 311, <https://doi.org/10.1002/2016GL071349>.
- Rodríguez, E., M. Bourassa, D. Chelton, J. T. Farrar, D. Long, D. Perkovic-Martin, and R. Samelson, 2019: The winds and currents mission concept. *Front. Mar. Sci.*, **6**, 438, <https://doi.org/10.3389/fmars.2019.00438>.
- Romero, L., 2019: Distribution of surface wave breaking fronts. *Geophys. Res. Lett.*, **46**, 10 463–10 474, <https://doi.org/10.1029/2019GL083408>.
- , L. Lenain, and W. K. Melville, 2017: Observations of surface wave–current interaction. *J. Phys. Oceanogr.*, **47**, 615–632, <https://doi.org/10.1175/JPO-D-16-0108.1>.
- , D. Hypolite, and J. C. McWilliams, 2020: Submesoscale current effects on surface waves. *Ocean Modell.*, **153**, 101662, <https://doi.org/10.1016/j.ocemod.2020.101662>.
- Suzuki, N., 2019: On the physical mechanisms of the two-way coupling between a surface wave field and a circulation consisting of a roll and streak. *J. Fluid Mech.*, **881**, 906–950, <https://doi.org/10.1017/jfm.2019.752>.
- Villas Bôas, A. B., and W. R. Young, 2020: Directional diffusion of surface gravity wave action by ocean macroturbulence. *J. Fluid Mech.*, **890**, R3, <https://doi.org/10.1017/jfm.2020.116>.
- , and Coauthors, 2019: Integrated observations and modeling of global winds, currents, and waves: Requirements and challenges for the next decade. *Front. Mar. Sci.*, **6**, 425, <https://doi.org/10.3389/fmars.2019.00425>.
- WAVEWATCH III Development Group, 2016: User manual and system documentation of WAVEWATCH III version 5.16. NOAA/NWS/NCEP/MMAB Tech. Note 329, 326 pp.